



Full Length Article

Designing multivalent NiMn-based layered nanosheets with high specific surface area and abundant active sites for solid-state hydrogen storage in magnesium hydride

Tao Zhong^{a,#}, Tian Xu^{b,#}, Liuting Zhang^{a,*}, Fuying Wu^a, Yiqun Jiang^c, Xuebin Yu^{b,*}

^aSchool of Energy and Power, Instrumental Analysis Center, Jiangsu University of Science and Technology, Zhenjiang 212003, China

^bDepartment of Materials Science, Fudan University, Shanghai 200433, China

^cMax Planck Institute for Iron Research, 40237 Düsseldorf, Germany

Received 6 February 2024; received in revised form 1 April 2024; accepted 19 April 2024

Available online 8 May 2024

Abstract

Catalytic doping of magnesium hydride (MgH_2) to improve its hydrogen ab/desorption kinetic properties is considered to be an effective and feasible method. In solid-phase catalysis, the extent of contact between the catalyst and the substrate determines the catalytic reaction in a great sense. With large specific surface area and abundant active sites, two-dimensional (2D) nanomaterials are promising catalysts for MgH_2 via providing numerous pathways for the diffusion and dissociation of hydrogen. In this regard, 2D NiMn-based layered double hydroxide and layered metallic oxide (LMO) are designed and introduced into MgH_2 to improve its hydrogen storage properties. Simultaneous enhancement in interfacial contact, desorption temperature and kinetics are achieved. The MgH_2 +9wt% Ni_3Mn -LMO composites begin to discharge hydrogen at only 190 °C and 6.10wt% H_2 could be charged in 600 s at 150 °C. The activation energy for de/hydrogenation is reduced by 42.43% and 46.56%, respectively, compared to pure MgH_2 . Even at a low operating temperature of 235 °C, the modified system was still able to release 4.44wt% H_2 in an hour, which has rarely been reported in previous studies. Microstructure observations and density functional theory calculations revealed that first, the hydrogen pumping effect of Mg_2Ni/Mg_2NiH_4 promotes the adsorption and desorption of hydrogen molecules on the surface of MgH_2 , second, MnO_x drew electrons from Mg_2Ni , producing a new Density of State structure with a lower d-bond center. This unique change further strengthens the Mg_2Ni/Mg_2NiH_4 pump effect on MgH_2 . Our work indicates that the application of 2D metal-based catalysts is a feasible and promising approach towards MgH_2 for solid-state hydrogen storage to meet technical and scientific requirements.

© 2024 Chongqing University. Publishing services provided by Elsevier B.V. on behalf of KeAi Communications Co. Ltd.

This is an open access article under the CC BY-NC-ND license (<http://creativecommons.org/licenses/by-nc-nd/4.0/>)

Peer review under responsibility of Chongqing University

Keywords: Hydrogen storage; Magnesium hydride; Layered metal oxides; Multivalent catalysis.

1. Introduction

The demand for clean energy has been increasing due to the depletion of fossil resources and growing environmental concerns. Hydrogen energy has attracted widespread attention because of its high combustion calorific value and abundant

sources [1–3]. Especially, the storage of hydrogen is crucial for its critical role in bridging hydrogen production and application [4,5]. Due to the excellent volumetric density (110.0 kg·m⁻³) and gravimetric hydrogen density (7.6wt%), MgH_2 has been widely investigated as a safe and efficient solid-state hydrogen storage material [6,7]. However, strong metal-hydrogen bonds and kinetic barriers restricted its further development and practical applications [8]. To address the above challenges, researchers have investigated various strategies to enhance the hydrogen storage capability of MgH_2 . Nanotechnology [9,10], alloying [11,12], and compositing [13,14] are

* Corresponding authors.

E-mail addresses: zhanglt89@just.edu.cn (L. Zhang), yuxuebin@fudan.edu.cn (X. Yu).

Tao Zhong and Tian Xu contributed equally.

demonstrated to effectively enhance the hydrogen storage performance.

Catalytic modification is also adopted as a feasible approach to improve the kinetic properties of MgH₂ by reducing the energy barrier for hydrogen ab/desorption [15–17]. Recently, the emergence of transition metal hydroxides/oxides with uniform distribution of active sites and the ability to undergo fast and reversible redox reactions lights great hope for pushing the performance of MgH₂ into advanced levels [18–21]. In our previous study [22], MOF-supported Nb₂O₅ nanoparticles were designed and the MgH₂+7wt%Nb₂O₅@MOF could release 6.2wt% hydrogen in 2.6 min at 275 °C. Samuel [23] et al. introduced Ni₆MnO₈ into MgH₂ by ball milling, and the multivalent state changes of Ni and Mn during hydrogen absorption and desorption were considered to be an essential factor in improving the hydrogen storage properties of MgH₂. Meng [24] et al. synthesized V₄Nb₁₈O₅₅ microspheres composed of tens of nanometer-sized nanoparticles, the distinctive molecular-scale Nb/V interface largely reduced the dehydrogenation energy barrier of MgH₂. Such oxides would be reduced to low-valent metal oxides or even zero-valent metals during the MgH₂ hydrogen storage process, resulting in a multi-element or multi-valent chemical environment. Separately, Large specific surface area is assumed to be important for the catalytic efficiency of dehydrogenation and hydrogenation. For example, Chen [25] et al. synthesized graphene-like TiO₂ (B) nanosheets with a monoclinic structure, the metallic Ti nanoparticles and wrinkled Ti₂O₃ generated during the hydrogen adsorption and desorption process created numerous boundary interfaces between MgH₂ and the catalysts to facilitate the hydrogen diffusion. Xian [26] et al. prepared a 2D bimetallic oxide TiNb₂O₇, which enabled MgH₂ to emit 7.0wt% H₂ when heated to 300 °C and a capacity retention of as high as 96% was achieved after 30 cycles. Furthermore, Ni is generally considered to react with Mg/MgH₂ to form Mg₂Ni/Mg₂NiH₄ during hydrogen uptake and release to lower the reaction barrier. On the other hand, Mn can easily form different oxides on the catalyst surface and undergo reversible transformation between different oxidation states, participating in the redox reaction and improving the catalytic activity.

Two-dimensional layered compounds are known as layered double hydroxides (LDHs) [27–29]. Heat treatment of LDHs can obtain corresponding metal oxides (layered metal oxides, LMOs) with an enlarged high active surface area while maintaining the original layered structure [30–32]. Inspired by the abundance of active sites in high specific surface area of 2D materials, the multivalent chemical environments of the oxides, and efficient catalysis by Ni and Mn, we prepared NiMn-LDH by a hydrothermal method, and NiMn-LMO was obtained by additional heat treatment. As expected, both of them improved the hydrogen storage performance of MgH₂, and kinetic analyses demonstrated that the catalytic performance of LMO was better than that of LDH. Microscopic characterization revealed that the generation of Mg₂Ni/Mg₂NiH₄, and the multivalent changes of Mn synergistically improved the performance of MgH₂.

2. Results and discussion

2.1. Microstructure of Ni₃Mn-LDH and NiMn-LMO

The synthetic procedure of Ni₃Mn-LDH and Ni₃Mn-LMO is illustrated in Fig. 1(a). The XRD patterns of Ni_xMn-LDH ($x = 1, 2, 3$) are shown in Fig. 1(b) and Fig. S1. The crystal structures of NiMn-LDH prepared by one-step hydrothermal method are all consistent with those reported in the literature [33], indicating the successful preparation of NiMn-LDH. The diffraction peaks at 37.32°, 43.36° and 62.99° of Ni₃Mn-LMO prepared after annealing treatment under argon atmosphere can be attributed to the (111), (210), and (220) faces of NiO (JCPDS No 75-0197). The remaining four diffraction peaks can be assigned to the (111), (220), (311), and (511) crystal planes of NiMn₂O₄ (JCPDS No 01-1110), which demonstrates that the annealed sample is composed of NiO and NiMn₂O₄ composite metallic oxides. Besides, the Rietveld refinement result of Ni₃Mn-LMO revealed that the mass percentage of NiO and NiMn₂O₄ are 88.9wt% and 11.1wt%, respectively. The transformation of Ni₃Mn-LDH into Ni₃Mn-LMO via pyrolysis is further confirmed by Raman spectroscopy (Fig. S2). Ni₃Mn-LDH exhibited Raman peaks typical of those belonging to LDH. While Ni₃Mn-LMO exhibited first-order and second-order optical phonon peaks characterized at \approx 565–616 and 1100 cm⁻¹, respectively, indicating the presence of NiO [34]. The chemical compositions and binding states of different atoms of the prepared Ni₃Mn-LDH and Ni₃Mn-LMO were analyzed by XPS as shown in Figs. S5, S6. The spectral peaks of C 1s, O 1s, Ni 2p, and Mn 2p can be observed from Fig. S5. Figure S6 (a) shows two major spin orbitals in the high-resolution Ni 2p spectra of 856.1 eV and 873.7 eV, which are attributed to the Ni 2p_{3/2} and Ni 2p_{1/2} binding energy of Ni. The spin energy interval is 17.6 eV, indicating that Ni²⁺ is in an oxidized state in both Ni₃Mn-LDH and Ni₃Mn-LMO [40]. The Mn 2p spectrum is shown in Fig. S6 (b) and consists of two main peaks, the 2p_{3/2} and 2p_{1/2} spin orbitals at 643.4 eV and 654.8 eV, respectively. In addition, the presence of three different oxidation states of Mn in both Ni₃Mn-LDH and Ni₃Mn-LMO can be obtained by using XPS split-peak fitting [44]. Therefore, it can be hypothesized that the presence of various valence forms of Mn may be beneficial for the hydrogen ab/desorption of MgH₂.

To confirm the geometric morphology of Ni₃Mn-LDH and Ni₃Mn-LMO, scanning electron microscopy (SEM) are employed in Fig. 1(d) and Fig. 1(e). It is obvious that the as-synthesized Ni₃Mn-LDH presents a hierarchical structure consisting of 2D layered nanosheets. SEM images of NiMn-LDH with different Ni/Mn ratios also showed the same geometrical shape (Fig. S3, S4). TEM images of Ni₃Mn-LDH similarly indicate ultrathin lattice structures (Fig. 2A (a, b)). As shown in Fig. 2A (c), the high-resolution transmission electron microscopy (HRTEM) image of Ni₃Mn-LDH exhibits a d spacing of 0.23 nm for the lattice stripes, which can be referred to selected regions of the (015) plane of Ni₃Mn-LDH. The electron diffraction (SAED) image (Fig. 2A (e)) shows

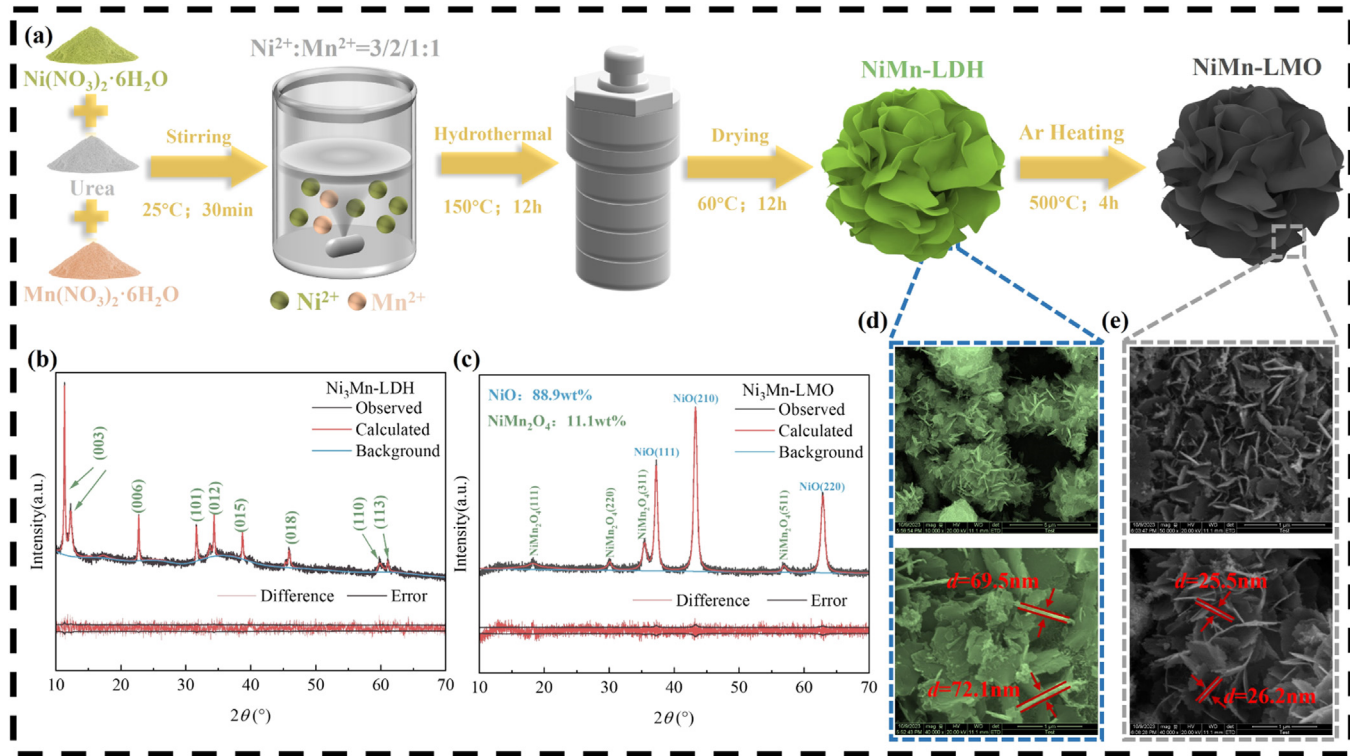


Fig. 1. Schematic diagram for the synthesis of Ni₃Mn-LDH and Ni₃Mn-LMO (a); XRD patterns and the refined results of Ni₃Mn-LDH (b), Ni₃Mn-LMO (c); SEM of Ni₃Mn-LDH (d), Ni₃Mn-LMO (e).

the reflected rings in the (110) and (015) planes of Ni₃Mn-LDH. The EDS mapping results in Fig. 1d further confirm the uniform distribution of Ni, Mn and O in Ni₃Mn-LDH. After heat treatment, Ni₃Mn-LMO maintained the layered structure (Fig. 1(e)). The removal of water molecules and anions between the LDH layers [35] leads to a lower degree of aggregation and thickness of the nanosheets and more surface defects. TEM images of Ni₃Mn-LMO similarly show that the laminar structure was preserved Fig. 2B (a, b). From Fig. 2B (c), lattice stripes with plane spacing of 0.208 nm and 0.253 nm corresponding to the (200) plane of NiO and (311) plane of NiMn₂O₄ are clearly observed, which is consistent with the XRD results. The SAED image (Fig. 2B (e)) further demonstrates that the (111), (222) planes of NiO and the (400), (440) planes of NiMn₂O₄. 400), (440) planes. In addition, the EDS mapping in Fig. 2B (d) also demonstrated that Ni, Mn and O were equally uniformly distributed in the Ni₃Mn-LMO catalyst. In addition, the N₂ adsorption-desorption isotherms (Fig. S7(a), Supporting Information) of both Ni₃Mn-LDH and Ni₃Mn-LMO are of typical iv-type, indicating the presence of meso- and micropores. Fig. S7(b) demonstrates the pore size distribution curves of Ni₃Mn-LDH and Ni₃Mn-LMO, and it is clear that Ni₃Mn-LMO produces more pore structures, leading to an increase in specific surface area. Some of these pore structures were generated by the conversion of stripped CO₃²⁻ to CO₂ under thermal treatment [31], indicating the generation of more catalytically active sites. The specific surface area and pore volume data calculated based on the Brunauer-Emmett - Teller (BET) method is summarized in Table S1.

Hereby, Ni₃Mn-LDH and Ni₃Mn-LMO composed of ultrathin nanosheets were successfully fabricated, which might provide a larger specific surface area and more catalytically active sites for hydrogen storage in MgH₂ [36].

2.2. Effect of NiMn-LDH and NiMn-LMO nanosheets on the dehydrogenation reaction of MgH₂

According to the non-isothermal hydrogen desorption curves in Fig. 3(a) and Fig. S9, the dynamic properties are all substantially improved as a result of catalyst addition. After considering both the amount of hydrogen release and the onset of dehydrogenation temperature, we selected a 9wt% addition ratio for the following experiments. The dehydrogenation temperature curves of the MgH₂ system with different molar ratio of Ni²⁺/Mn²⁺ additions reveal that the onset and terminal dehydrogenation temperatures of the modified MgH₂ system were all greatly reduced. Specifically, as the molar ratio of Ni²⁺ increases, the onset dehydrogenation temperature of MgH₂ decreases gradually and the dehydrogenation rate is accelerated. Of these, MgH₂+9wt% Ni₃Mn-LDH has the lowest onset dehydrogenation temperature with the most rapid dehydrogenation rate. It started discharging at 210 °C, which is 140 °C lower than the pristine MgH₂, and can discharge 6.63wt% of H₂ at 350 °C, where pure MgH₂ only began to release hydrogen. After annealing, the Ni₃Mn-LMO further reduced the starting dehydrogenation temperature of MgH₂ to 190 °C and the dehydrogenation rate was ulteriorly accelerated (Fig. 3(b)).

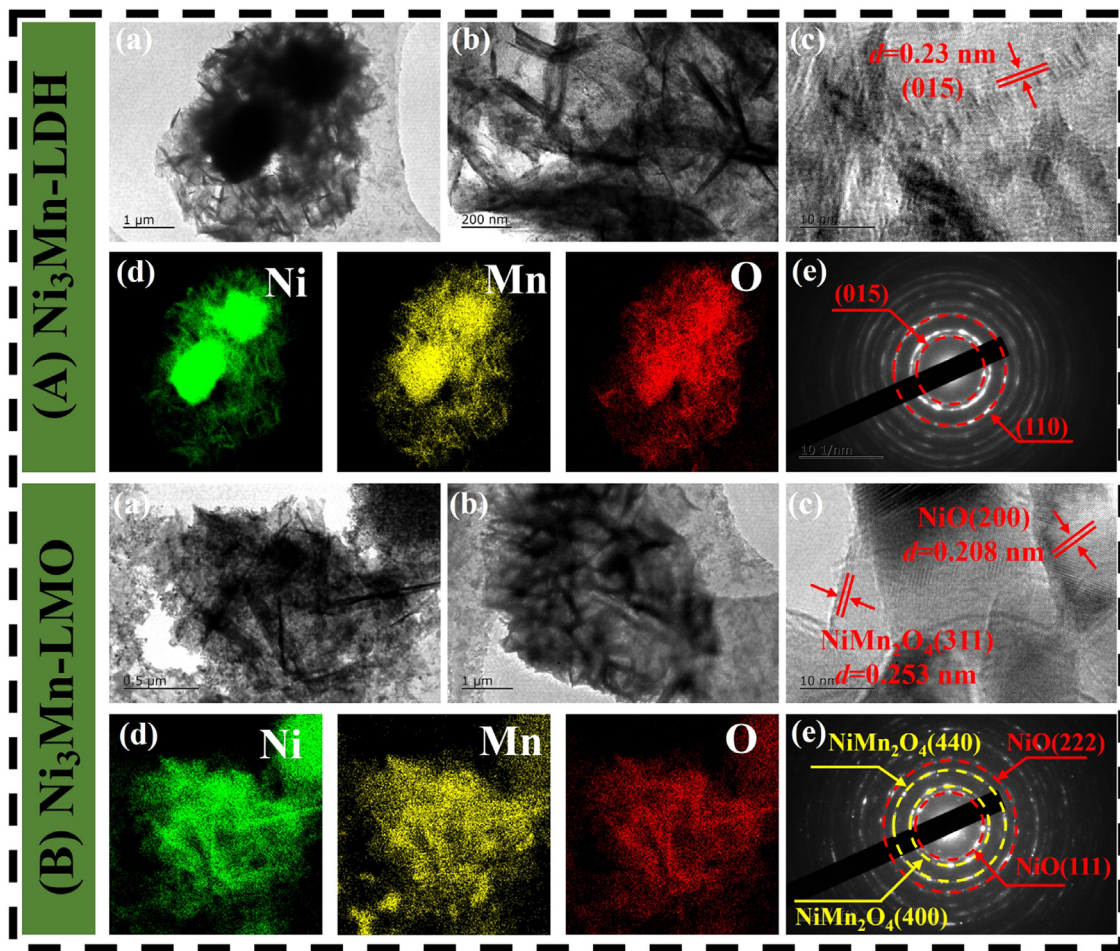


Fig. 2. (A): TEM images (a, b), HRTEM images (c), elemental mapping (d) and SAED (e) of $\text{Ni}_3\text{Mn-LDH}$; (B): TEM images (a, b), HRTEM images (c), elemental mapping (d) and SAED (e) of $\text{Ni}_3\text{Mn-LMO}$.

The isothermal dehydrogenation curves between the modified MgH_2 with pristine MgH_2 were compared in Fig. 3(c-f). Generally, the dehydrogenation performance of $\text{MgH}_2+9\text{wt\% Ni}_3\text{Mn-LMO}$ was superior to that of $\text{MgH}_2+9\text{wt\% Ni}_3\text{Mn-LDH}$ at all temperatures, while the pristine MgH_2 performed worse than both. Both $\text{MgH}_2+9\text{wt\% Ni}_3\text{Mn-LDH}$ and $\text{MgH}_2+9\text{wt\% Ni}_3\text{Mn-LMO}$ can discharge hydrogen at temperatures as low as 235 °C, with 3.20wt% and 4.44wt% of hydrogen in 60 min, respectively. Raising the temperature to 250 °C, the dehydrogenation kinetics became much faster. Specifically, as shown in Fig. 3(f) and its inset, the rate of $\text{MgH}_2+9\text{wt\% Ni}_3\text{Mn-LMO}$ for releasing 5wt% H_2 is 4.57 times larger than that of $\text{MgH}_2+9\text{wt\% Ni}_3\text{Mn-LDH}$. Remarkably, $\text{MgH}_2+9\text{wt\% Ni}_3\text{Mn-LMO}$ was able to emit 6.59wt% H_2 in just 5 min at 295 °C, while at the same temperature, $\text{MgH}_2+9\text{wt\% Ni}_3\text{Mn-LDH}$ required 10 min to release the same amount of H_2 .

In order to gain insight into the mechanism of dehydrogenation kinetics, isothermal dehydrogenation curves of MgH_2 , $\text{MgH}_2+9\text{wt\% Ni}_3\text{Mn-LDH}$, and $\text{MgH}_2+9\text{wt\% Ni}_3\text{Mn-LMO}$ were fitted to the Chou-model [37] to derive the rate-controlling steps of the dehydrogenation reaction. The dehydrogenation process of MgH_2 in the Chou-model consists

mainly of two models, penetration and diffusion, with the penetration model being the slower step in the hydrogen release process compared to the diffusion model. As shown in Fig. 4(a-b) and Fig. S10(a-b), the penetration model dominates the rate control step for pristine MgH_2 as well as for $\text{MgH}_2+9\text{wt\% Ni}_3\text{Mn-LDH}$, which is in accordance with the experimental results. For $\text{MgH}_2+9\text{wt\% Ni}_3\text{Mn-LMO}$, the rate control step of the Chou-model transforms into a diffusion step (Fig. 4(c) and Fig. S10(c)), which also provides strong evidence that the catalytic performance with $\text{Ni}_3\text{Mn-LMO}$ is superior to that of $\text{Ni}_3\text{Mn-LDH}$. In addition, we calculated the dehydrogenation activation energies of MgH_2 , $\text{MgH}_2+9\text{wt\% Ni}_3\text{Mn-LDH}$, and $\text{MgH}_2+9\text{wt\% Ni}_3\text{Mn-LMO}$ using the Arrhenius equation [38] to further illustrate the improvement on kinetics. The results are shown in Fig. 4(d) and Fig. S12(a-c). The dehydrogenation activation energy of pristine MgH_2 was $150.90 \pm 2.58 \text{ kJ}\cdot\text{mol}^{-1}$, which was reduced to $103.68 \pm 5.24 \text{ kJ}\cdot\text{mol}^{-1}$ with the addition of 9wt% $\text{Ni}_3\text{Mn-LDH}$, and the dehydrogenation activation energy was further reduced with the addition of 9wt% $\text{Ni}_3\text{Mn-LMO}$ to $86.88 \pm 6.48 \text{ kJ}\cdot\text{mol}^{-1}$. The greatly reduced activation energy further supports the excellent hydrogen desorption capability of $\text{MgH}_2+9\text{wt\% Ni}_3\text{Mn-LMO}$. In particular, the dehy-

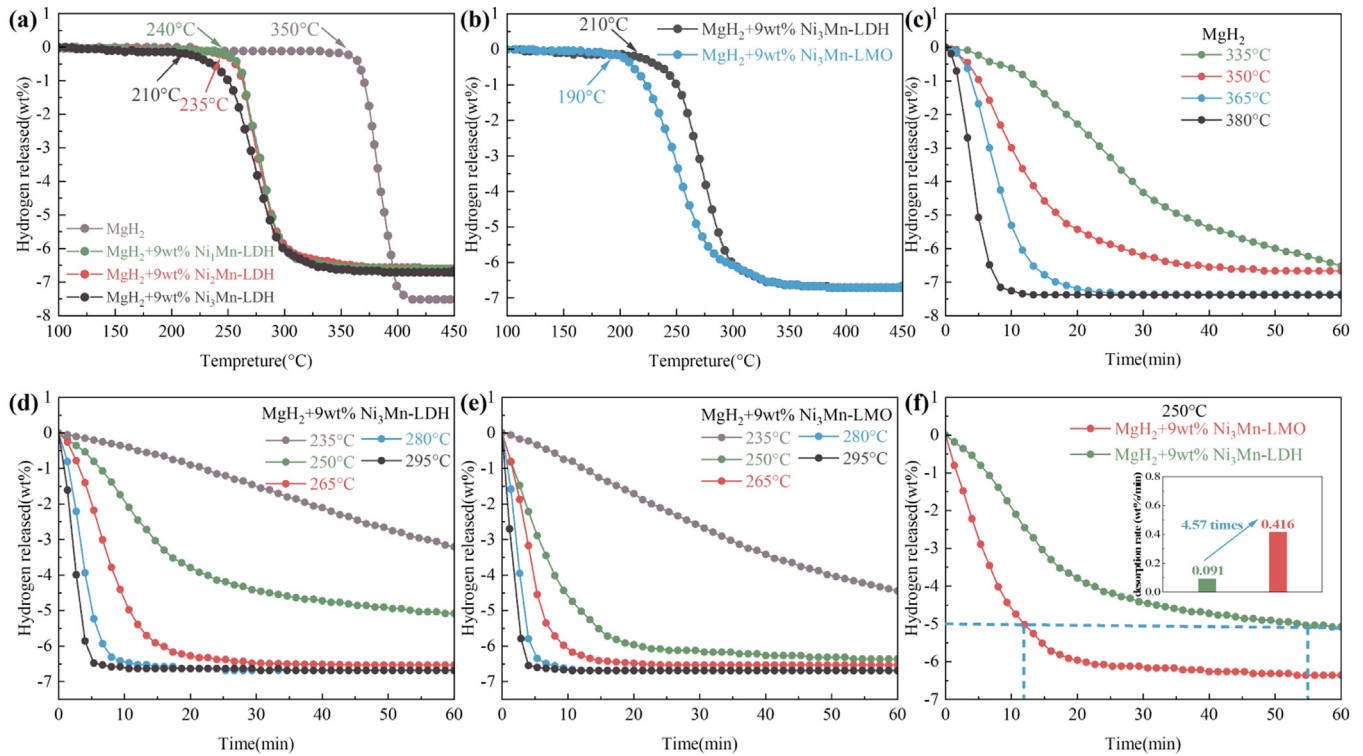


Fig. 3. Desorption curves of MgH₂, MgH₂+9wt% Ni_xMn-LDH ($x = 1, 2, 3$) (a), MgH₂+9wt% Ni₃Mn-LDH, and MgH₂+9wt% Ni₃Mn-LMO in non-isothermal mode (b); desorption curves of MgH₂ (c), MgH₂+9wt% Ni₃Mn-LDH (d), MgH₂+9wt% Ni₃Mn-LMO (e), MgH₂+9wt% Ni₃Mn-LDH and MgH₂+9wt% Ni₃Mn-LMO at 250 °C in isothermal mode (f).

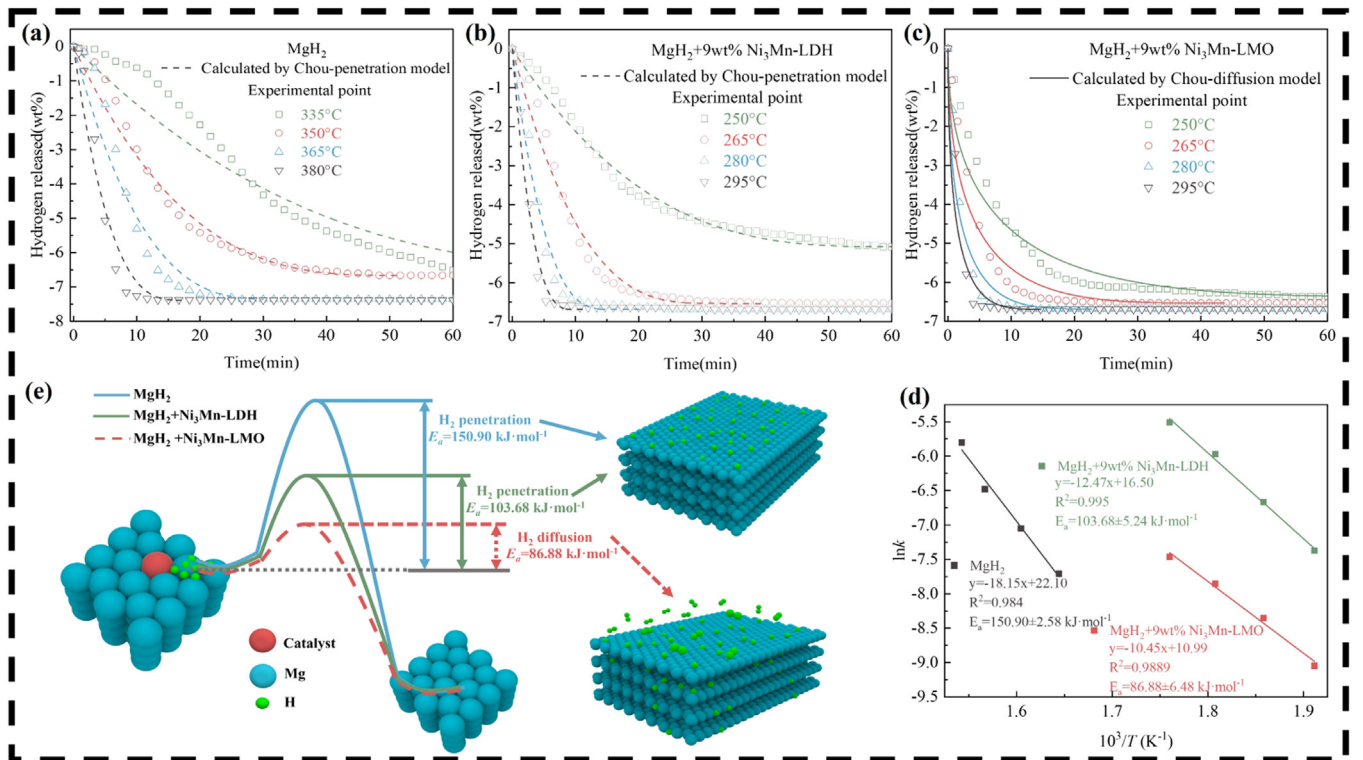


Fig. 4. Experimental points of hydrogen release and curves obtained by Chou-model prediction for MgH₂ (a), MgH₂+9wt% Ni₃Mn-LDH (b), and MgH₂+9wt% Ni₃Mn-LMO (c) at different temperatures; corresponding dehydrogenation activation energy (d); mechanism diagram of hydrogen penetration and diffusion (e).

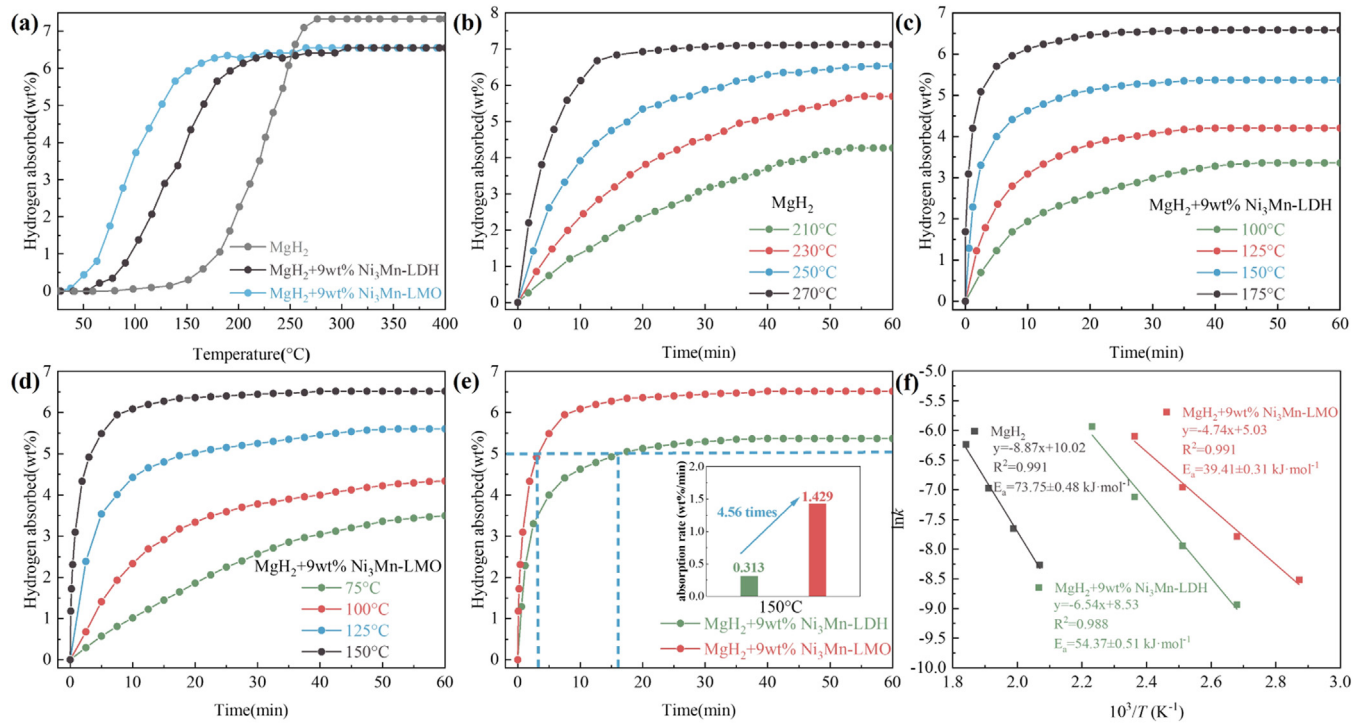


Fig. 5. Absorption curves of MgH₂, MgH₂+9wt% Ni₃Mn-LDH, and MgH₂+9wt% Ni₃Mn-LMO in non-isothermal mode (a); absorption curves of MgH₂(b), MgH₂+9wt% Ni₃Mn-LDH (c), MgH₂+9wt% Ni₃Mn-LMO (d), MgH₂+9wt% Ni₃Mn-LDH and MgH₂+9wt% Ni₃Mn-LMO at 150 °C in isothermal mode (e); corresponding rehydrogenation activation energy (f).

drogenation activation energy is much lower than that of other magnesium matrix composites (Table S2), which explains the source of its excellent hydrogen release properties. Combining the Chou-model and the activation energy, Fig. 4(e) vividly depicts the hydrogen release of MgH₂ in different environments. It can be summarized that the layered metallic oxide is an efficient catalyst that well enhanced the dehydrogenation ability of MgH₂.

2.3. Effect of NiMn-LDH and NiMn-LMO nanosheets on the hydrogen absorption reaction of MgH₂

Hydrogen absorption experiments including non-isothermal and isothermal hydrogenation were performed on MgH₂, MgH₂+9wt% Ni₃Mn-LDH, and MgH₂+9wt% Ni₃Mn-LMO to evaluate the hydrogen absorption performance. Fig. 5(a) illustrates the non-isothermal hydrogen absorption curves, which show the onset of hydrogen absorption of pristine MgH₂ was 120 °C. With the introducing of 9wt% Ni₃Mn-LDH and 9wt% Ni₃Mn-LMO, the onset hydrogen absorption temperatures decreased to 50 °C and 28 °C, respectively. The results of isothermal hydrogen absorption tests performed at different temperatures are shown in Fig. 5(b-e). The fully dehydrogenated MgH₂+9wt% Ni₃Mn-LDH could absorb 3.36wt% H₂ in 60 min at 100 °C, while MgH₂+9wt% Ni₃Mn-LMO could charge 4.34wt% H₂ at identical condition, and 3.49wt% H₂ could be absorbed in 60 min at a lower temperature of 75 °C. The hydrogen absorption rates were compared at the same temperature of 150 °C (Fig. 5(e)). For

the same absorption of 5wt% H₂, the rate of MgH₂+9wt% Ni₃Mn-LMO is 4.56 times higher than that of MgH₂+9wt% Ni₃Mn-LDH. Encouragingly, MgH₂+9wt% Ni₃Mn-LMO can charge even as much as 6.1wt% of H₂ at 150 °C in only 10 min. In contrast, undoped MgH₂ requires a higher operating temperature to achieve the same rehydrogenation performance of the doped samples.

The rehydrogenation activation energies of MgH₂, MgH₂+9wt% Ni₃Mn-LDH, and MgH₂+9wt% Ni₃Mn-LMO calculated by the Arrhenius equation are shown in Fig. 5(f) and Fig. S12(d-f). The activation energy for rehydrogenation of pristine MgH₂ was $73.75 \pm 0.48 \text{ kJ} \cdot \text{mol}^{-1}$, which decreased to $54.37 \pm 0.51 \text{ kJ} \cdot \text{mol}^{-1}$ and $39.41 \pm 0.31 \text{ kJ} \cdot \text{mol}^{-1}$ after the addition of 9wt% Ni₃Mn-LDH and 9wt% Ni₃Mn-LMO, respectively. In order to understand the rate-controlling steps of the rehydrogenation reaction, isothermal hydrogen absorption curves were fitted with the Chou-model as well. As shown in Fig. S11, the hydrogen uptake of pristine MgH₂ is mainly dominated by the penetration equation at lower temperatures of 210 °C, 230 °C, and 250 °C, and the dominant step changes from penetration to diffusion as the temperature rises up to 270 °C. This is due to the fact that the hydrogen uptake process of MgH₂ is more sensitive to temperature. In the case of MgH₂+9wt% Ni₃Mn-LDH, the controlling step is dominated by penetration at 100 °C, whereas it changes from penetration to diffusion at the low temperature of 150 °C. Regarding MgH₂+9wt% Ni₃Mn-LMO, the main step controlling its rehydrogenation, also at 100 °C, is the diffusion model, which is consistent with the results of the rehydrogenation

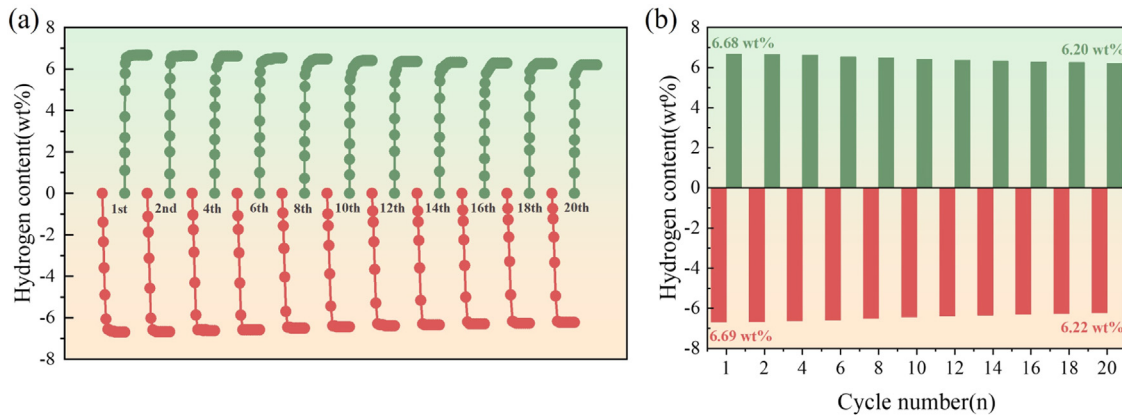


Fig. 6. Isothermal dehydrogenation/hydrogenation curves of $\text{MgH}_2 + 9\text{wt\% Ni}_3\text{Mn-LMO}$ composite at 295 °C for 20 cycles.

experiments in Fig. 4. The above results support strongly the conclusion that the hydrogen uptake of $\text{MgH}_2 + 9\text{wt\% Ni}_3\text{Mn-LMO}$ is superior to that of $\text{MgH}_2 + 9\text{wt\% Ni}_3\text{Mn-LDH}$.

2.4. Influence of $\text{Ni}_3\text{Mn-LDH}$ and $\text{Ni}_3\text{Mn-LMO}$ on thermodynamics of MgH_2

The thermodynamic properties of $\text{Ni}_3\text{Mn-LDH}$ and $\text{Ni}_3\text{Mn-LMO}$ modified MgH_2 were further investigated by determining the equilibrium hydrogen pressures of MgH_2 , $\text{MgH}_2 + 9\text{wt\% Ni}_3\text{Mn-LDH}$ and $\text{MgH}_2 + 9\text{wt\% Ni}_3\text{Mn-LMO}$ at different temperatures as shown in Fig. S13(a-c). The desorption plateau pressures of MgH_2 were 2.53, 4.66, 9.82, and 16.78 bar at 325 °C, 350 °C, 375 °C, and 400 °C. The plateau pressures of $\text{MgH}_2 + 9\text{wt\% Ni}_3\text{Mn-LDH}$ were 1.61, 3.06, 5.86 and 10.54 bar at 300 °C, 325 °C, 350 °C, and 375 °C, respectively, while the plateau pressures of $\text{MgH}_2 + 9\text{wt\% Ni}_3\text{Mn-LMO}$ had plateau pressures of 1.55, 2.94, 5.50 and 10.24 bar, respectively. The corresponding enthalpies of hydrogen decomposition (ΔH) were calculated by the Van't Hoff equation as shown in Fig. S13(d). The value of ΔH for MgH_2 was estimated to be $83.08 \pm 2.43 \text{ kJ/mol}$. However, even after the addition of $\text{Ni}_3\text{Mn-LDH}$ ($78.04 \pm 2.17 \text{ kJ/mol}$) and $\text{Ni}_3\text{Mn-LMO}$ ($76.84 \pm 0.91 \text{ kJ/mol}$) the calculated value of ΔH was also slightly lower than that of the prepared MgH_2 . Therefore, like other previously reported catalysts $\text{Ni}_3\text{Mn-LDH}$ and $\text{Ni}_3\text{Mn-LMO}$ can significantly improve the kinetic properties of MgH_2 , but have little effect on the thermodynamic properties of MgH_2 .

2.5. Cycling feature of $\text{MgH}_2 - 9\text{wt\% Ni}_3\text{Mn-LMO}$

The cycling characteristics of composites are considered to be an important indicator for assessing hydrogen storage performance and are necessary for practical applications. Since $\text{MgH}_2 + 9\text{wt\% Ni}_3\text{Mn-LMO}$ has better hydrogen storage properties than $\text{MgH}_2 + 9\text{wt\% Ni}_3\text{Mn-LDH}$ or pristine MgH_2 , we carried out up to 20 isothermal hydrogen ab/desorption experiments at 295 °C to investigate the cyclic stability of $\text{MgH}_2 + 9\text{wt\% Ni}_3\text{Mn-LMO}$. After 20 cycles, the

$\text{MgH}_2 + 9\text{wt\% Ni}_3\text{Mn-LMO}$ composite was still able to desorb and absorb 6.22wt%, 6.20wt% H_2 , which indicate excellent reversibility and stability of the $\text{MgH}_2 + 9\text{wt\% Ni}_3\text{Mn-LMO}$ composite. The decrease in reversible hydrogen storage capacity is due to the fact that nanoscale MgH_2 is highly susceptible to particle aggregation and growth during hydrogen uptake and release, leading to capacity decay and kinetic degradation. In addition, as the number of cycles increases, a small portion of the Mg nucleation and growth leads to the inability to be hydrogenated, which will directly lead to a decrease in the cycling capacity (Fig. 6).

2.6. Mechanism for the improved hydrogen storage properties

To identify the catalytic mechanism of LMO in composites, the microstructural changes of the materials in the process of dehydrogenation and rehydrogenation were investigated in detail. XRD results demonstrate that reversible transformations of MgH_2 and Mg dominate during hydrogen desorption and adsorption (Fig. 7(a, b)). It is noteworthy that due to the high activity of LMO, it reacts with MgH_2 during ball milling, leading to the appearance of peaks belonging to metallic nickel. During the hydrogen release process, MgH_2 further reacts with metal Ni to form Mg_2Ni , which in the subsequent rehydrogenation reacts with hydrogen to form Mg_2NiH_4 . The generation of Mg_2Ni and Mg_2NiH_4 increases the free energy and reactivity of the system, which provides extra energy for the resolution and adsorption of hydrogen. In addition, it acts as a low-energy barrier region for hydrogen diffusion, reducing the hydrogen ad/desorption reaction energy barriers of MgH_2 . In addition, the XRD pattern of the rehydrogenated state after 20 cycles is shown in Fig. S15 (a), the appearance of the Mg peaks confirms the decrease of the capacity during the cycling process.

However, no diffraction peaks were found for compounds about Mn, which may be due to the in situ reduction of Mn or its low content [24]. Therefore, the changes of Ni and Mn in LMO were further analyzed by XPS measurement. It should be noted that during the characterization of XPS,

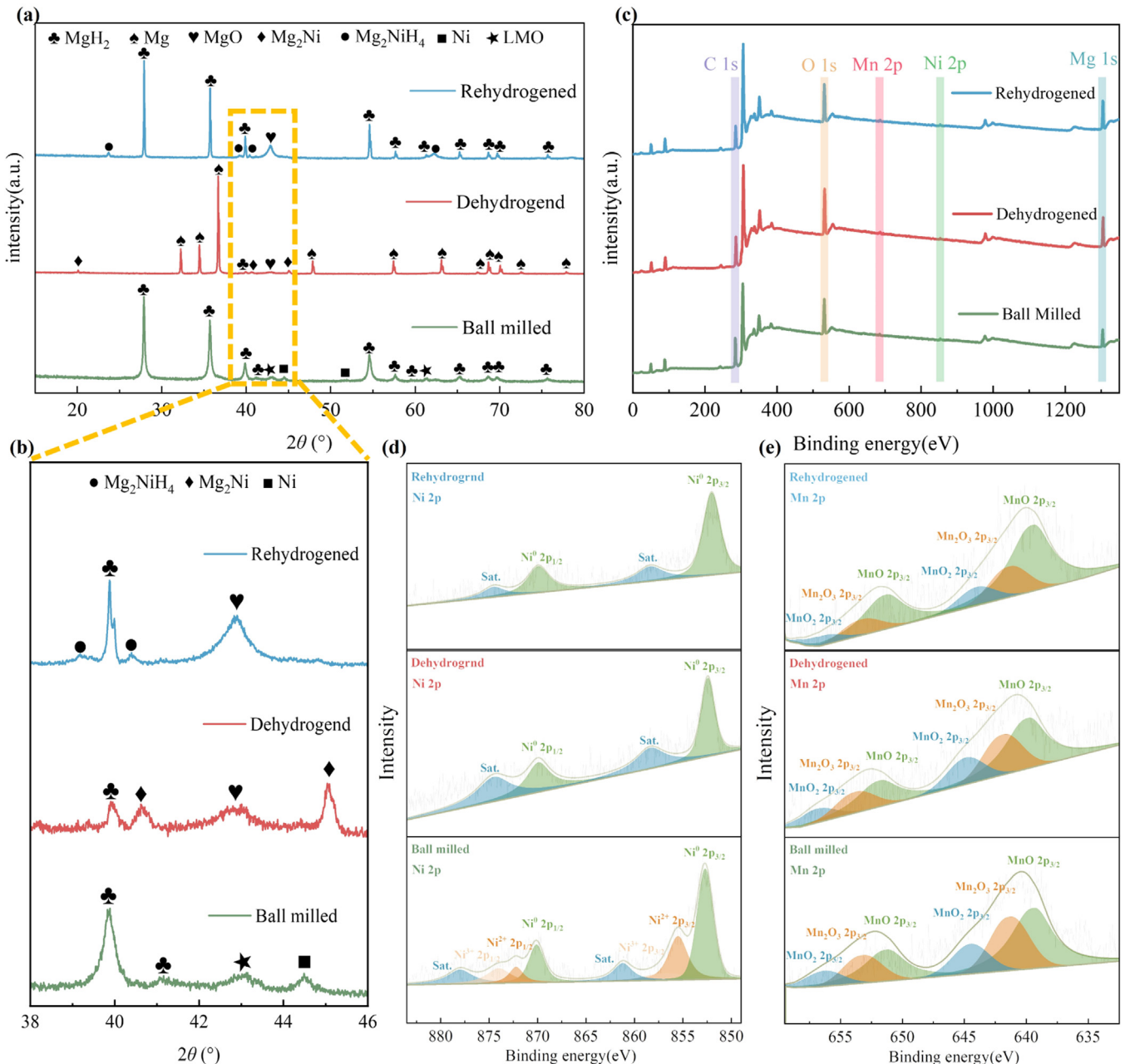


Fig. 7. XRD patterns of MgH_2 +9wt% Ni_3Mn -LMO composite: ball milled, dehydrogenated, rehydrogenated (a) and its local enlargement (b), Full region XPS spectra of MgH_2 +20wt% Ni_3Mn -LMO composite: ball milled, dehydrogenated (c), Ni 2p (d) and Mn 2p XPS (e) spectra of MgH_2 +20wt% Ni_3Mn -LMO after milled, dehydrogenated, and rehydrogenated.

the percentage of catalyst was increased to 20wt% in order to ensure the effective identification of the Ni and Mn states. The non-isothermal hydrogen release curves with the addition of 20wt% LMO are comparable to the addition of 9wt% LMO (Fig. S14), suggesting that the evolution of Ni and Mn in the reaction is consistent. Full region XPS spectra displayed the signals of Mg 1s, Ni 2p, Mn 2p, O 1s, and C 1s in Fig. 7(c). After ball milling, the peaks of Ni^0 2p (852.7 and 870.1 eV) [39] can be clearly detected by XPS (Fig. 7(d)), indicating that metallic Ni was generated during the ball milling process, which is in agreement with the results of XRD. The peaks of Ni^{2+} 2p (855.5 and 872.2 eV)

and Ni^{3+} 2p (856.86 and 874 eV) [40,41] belong to unreacted NiO and NiMn_2O_4 . After dehydrogenation, peaks belonging to Ni^{2+} and Ni^{3+} disappeared due to reduction, with Ni^0 2p (852.4 and 869.8 eV) belonging to Mg_2Ni observed in Ni 2p XPS spectra [42]. After rehydrogenation, the peaks of Ni^0 2p (852.4 and 869.8 eV) belonging to Mg_2NiH_4 still existed [43]. The evolution of Mg_2Ni and Mg_2NiH_4 agrees well with the XRD results. In contrast, the different valence states of Mn in LMO were consistently observed during the whole reaction (Fig. 7(e)). In the ball-milled state, peaks belonging to MnO (640.0 and 650.3 eV), Mn_2O_3 (642.2 and 652.5 eV), and MnO_2 (644.5 and 654.8 eV) can be observed [44,45]. Af-

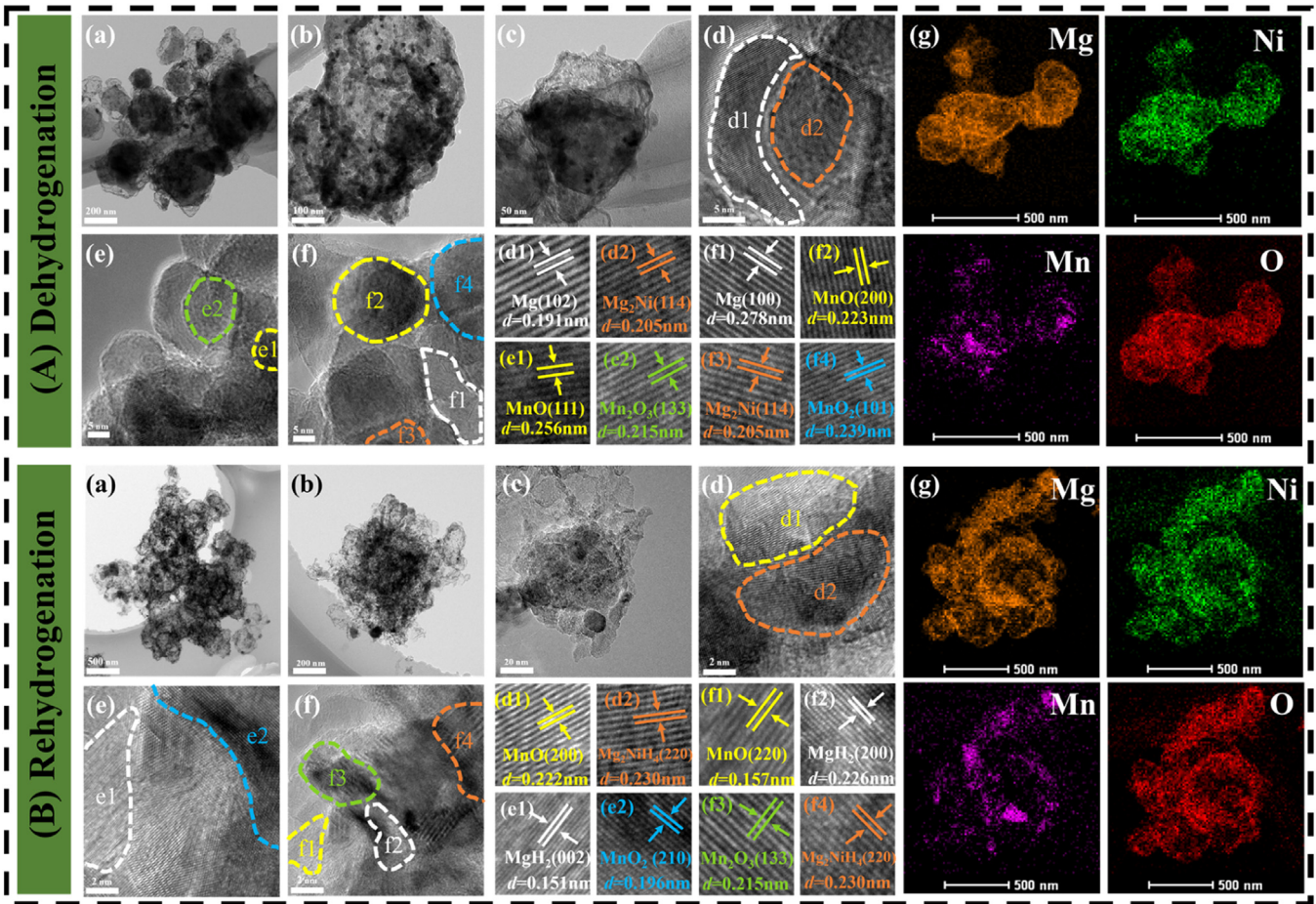


Fig. 8. (A): TEM images (a-c), HRTEM images (d-f), and elemental mapping (g) of MgH₂+9wt% Ni₃Mn-LMO after dehydrogenation; (B): TEM images (a-c), HRTEM images (d-f), and elemental mapping (g) of MgH₂+9wt% Ni₃Mn-LMO after rehydrogenation.

ter subsequent dehydrogenation and rehydrogenation, partial reduction of Mn³⁺ and Mn⁴⁺ leads to an increase in Mn²⁺ content. The XPS of the rehydrogenated state after 20 cycles is also shown in Fig. S15 (b-d), the same Ni⁰ 2p (852.4 and 869.8 eV) peaks belonging to Mg₂NiH₄ are observed as in the rehydrogenated state. While after 20 cycles, a further increase in Mn²⁺ content was observed in the Mn 2p XPS spectra due to the reducing effect. Consequently, it could be concluded that the multivalent state changes of Ni and Mn in LMO could promote the process of H₂ desorption and adsorption of MgH₂.

Subsequently, the evolution of the microstructure of MgH₂ catalyzed by LMO was investigated using TEM and HRTEM (Fig. 8(A, B) and Fig. S16, S17). The TEM and HRTEM of ball-milled MgH₂+9wt% Ni₃Mn-LMO is displayed in Fig. S16, in the same results as the XRD that besides the observation of MgH₂, facets belonging to Ni are also observed. The microscopic morphology of MgH₂ after dehydrogenation is shown in Fig. 8A(a-c). It can be observed that the LMO nanosheets introduced into MgH₂ are fragmented into fine sheets. From the HRTEM images (Figs. 8A(d, f) and 8B(e, f)), the (102), (100) planes corresponding to Mg and the (002), (200) planes of MgH₂ can be observed. This indicates that

the reversible transformation of Mg and MgH₂ occurs during the H₂ desorption and adsorption process, which is in good agreement with the XRD results. During the initial dehydrogenation process, HRTEM images (Fig. 8A(d, f)) illustrate the obvious interplanar distance of 0.191 nm and 0.278 nm, which belong to the (102) and (100) planes of Mg. It's worth noting that lattice spacings of 0.205 nm could be indexed to the (114) planes of Mg₂Ni, in supportive with the XRD and XPS results. After the hydrogenation process, new lattice spacings of 0.230 nm can be observed (Fig. 8B(d, f)), pointing to the (220) planes of Mg₂NiH₄. Furthermore, the dehydrogenated and rehydrogenated HRTEM image show distinct lattice spacings of 0.157, 0.215, and 0.196 nm, which can be pointed to the (220) face of metallic MnO, the (133) face of Mn₂O₃, and the (210) face of MnO₂, respectively, which are also in good agreement with the XPS results. The TEM pattern of the rehydrogenated state after 20 cycles is shown in Fig. S17. It can be observed that after 20 cycles, the grain size of MgH₂ has grown, which is the reason for the decay of hydrogen storage after cycling. In addition, the results of the EDS mapping (Fig. 8(A, B)(g)) revealed that elements of Ni, Mn, and O were uniformly dispersed on the surface of Mg and MgH₂, which confirms that the LMO has suffi-

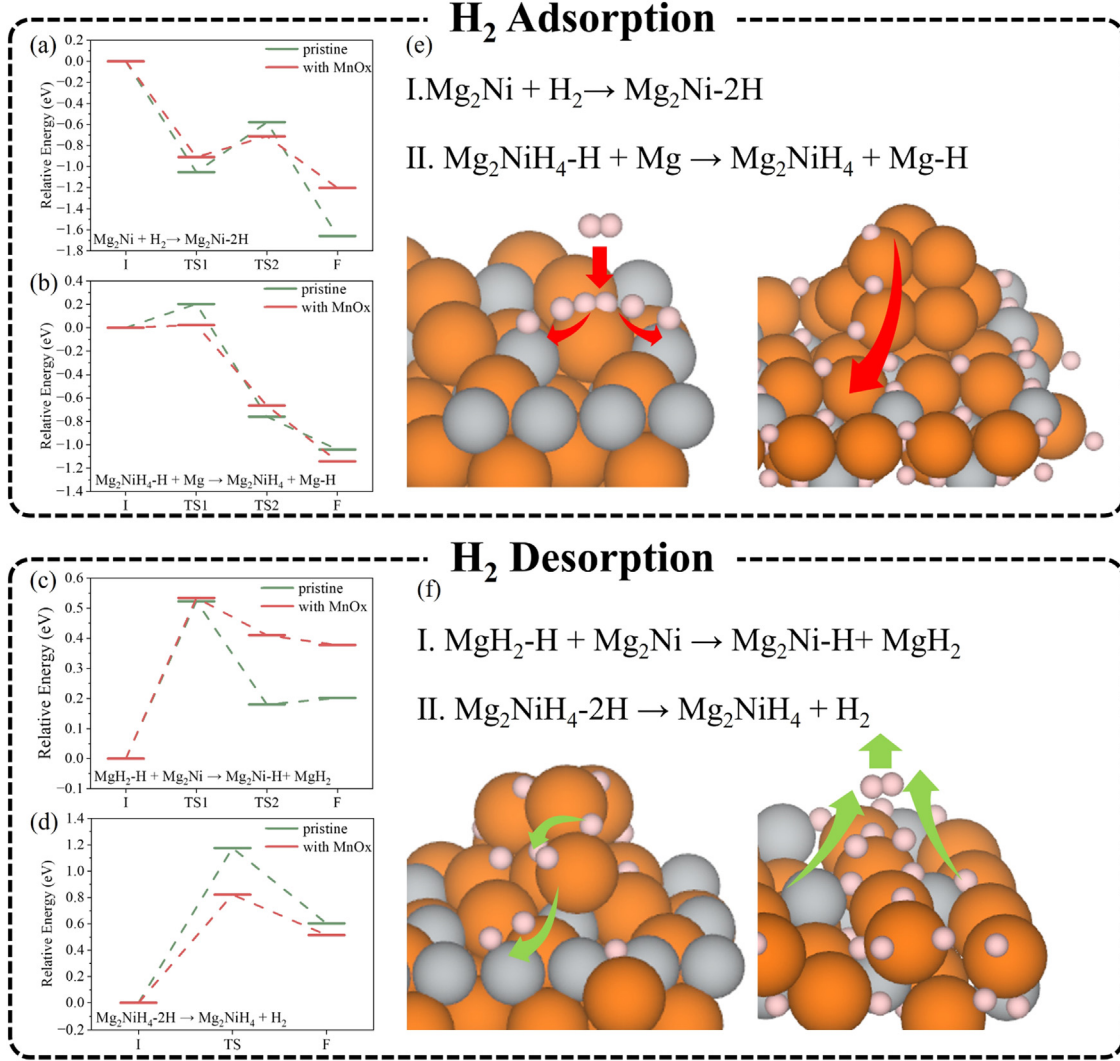


Fig. 9. (a-d) Energy change curves for different reaction processes; stepwise reaction functions and schematic 3D model for (e) H₂ adsorption and (f) H₂ desorption.

cient contact with Mg/MgH₂ during the reaction process. The in-situ formed Mg₂Ni/Mg₂NiH₄ and Mn species of (MnO, Mn₂O₃, MnO₂) collaborate to exhibit a significant impact in the catalysis procedure to boost the kinetics of the Mg/MgH₂ system.

Theoretical calculations based on Density Functional Theory (DFT) are utilised to elucidate the catalytic mechanism of NiMn-LMO in the hydrogen storage of MgH₂. The aforementioned NiMn-LMO acts in dual capacities: as a hydrogen pump and as an efficient catalyst. The presence of Mg₂Ni facilitates a more straightforward two-step hydrogen storage reaction, as opposed to a direct reaction with Mg. Concurrently, MnO_x catalysis expedites these processes, making them more stable and efficient. A two-step model is employed to simulate both adsorption and desorption reactions (Fig. 9(e, f)). Lower energy barriers are evident in models with MnO_x, consistent with experimental findings (Fig. 9(e, f)). Influenced by MnO_x, the reaction's intermediary product, Mg₂Ni-H, exhibits a higher total energy. This typically indicates a less

stable structure, predisposed to easy bond dissociation, which results in a quicker hydrogen transformation from Mg₂NiH₄ to Mg during H₂ adsorption, and simpler dehydrogenation in the desorption process. A comparative analysis was conducted on the state structure of Mg₂Ni with and without MnO_x, to further understand why MnO_x can weaken the bond between the catalyst and hydrogen. Density of State (DOS) analysis reveals a significant change in state structure induced by MnO_x (Fig. S19(a)). More specifically, Mg₂Ni with MnO_x has a lower d-bond center at -1.581 eV compared to -0.941 eV of pure Mg₂Ni (Fig. S18 (b)). According to the d-bond theory proposed by Norskov [46], a lower d-bond center forms a lower antibonding orbital, which is more easily filled by electrons, thereby reducing the overall bonding strength. The alteration in the state structure is attributed to the electron exchange between MnO_x and Mg₂Ni, visible in Fig. S19. Table S3 provides a detailed charge distribution among each atom. In comparison to an isolated situation, MnO_x draws 6.395 electrons from Mg₂Ni, causing the aforementioned state struc-

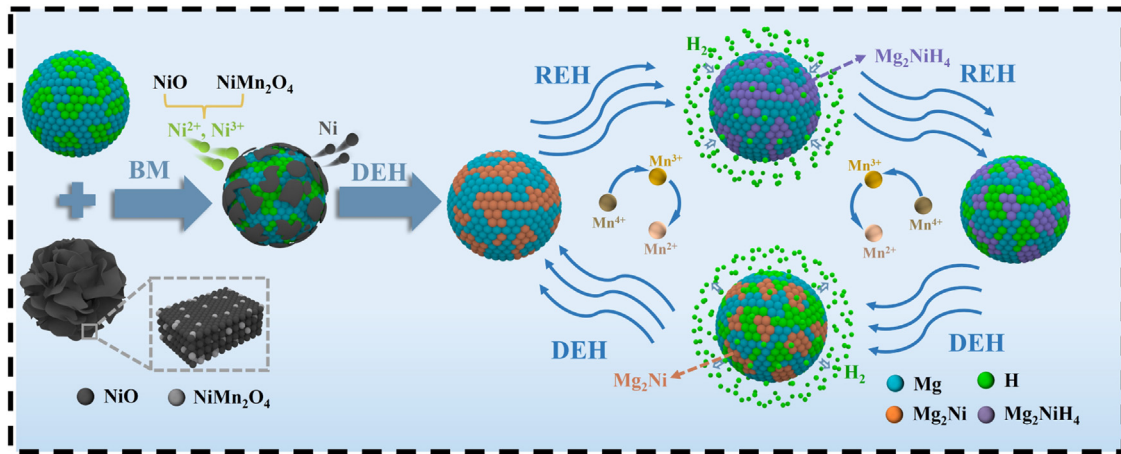


Fig. 10. Mechanism diagram of dehydrogenation and rehydrogenation of the $\text{Ni}_3\text{Mn-LMO}$ catalyzed MgH_2/Mg system.

ture change. In summary, MnO_x draws electrons from Mg_2Ni , producing a new DOS structure with a lower d-bond center. This unique change weakens the bond between hydrogen and Mg_2Ni pump. Macroscopically, this results in a more moderate hydrogen absorption and release temperature, along with a faster rate.

Combined with XRD, XPS, TEM, and DFT analysis, the catalytic mechanism is presented in Fig. 10. The LMO nanosheets with large specific surface area are in close contact with MgH_2 , which creates a favorable environment (a large number of activation sites and diffusion channels) for the catalysis of solid-state dehydrogenation/hydrogenation reactions. Ni produced by reduction during ball milling reacts well with MgH_2 during dehydrogenation to produce Mg_2Ni , which is converted to Mg_2NiH_4 during rehydrogenation. The formation of $\text{Mg}_2\text{Ni}/\text{Mg}_2\text{NiH}_4$ acts as a “hydrogen pump” to promote the hydrogen storage process in MgH_2 [47,48]. Specifically, the enthalpy of formation of $\text{Mg}_2\text{Ni}/\text{Mg}_2\text{NiH}_4$ is lower than that of Mg/MgH_2 , and thus takes the lead to react with hydrogen during hydrogen absorption and desorption. In addition, $\text{Mg}_2\text{Ni}/\text{Mg}_2\text{NiH}_4$ can provide a large number of low-energy barrier H diffusion channels to accelerate the adsorption and desorption of hydrogen. Meanwhile, the multivalent chemical environment of Mn during hydrogen absorption and desorption also greatly contributes to the kinetic properties of MgH_2 . LMO owns the advantages of high specific surface area and abundant active sites of 2D materials. Besides, the in-suit generated $\text{Mg}_2\text{Ni}/\text{Mg}_2\text{NiH}_4$ served as nano-hydrogen pumps and the multivalent state of Mn accelerated the electron transfer during catalysis. Therefore, LMO exerts excellent catalytic effect on Mg-based hydrogen storage materials.

3. Conclusion

In this work, 2D NiMn-LDH and NiMn-LMO were successfully synthesized. Both $\text{Ni}_3\text{Mn-LDH}$ and $\text{Ni}_3\text{Mn-LMO}$ significantly improved the hydrogen storage properties of MgH_2 . In particular, $\text{MgH}_2+\text{Ni}_3\text{Mn-LMO}$ has better hydro-

gen uptake and discharge kinetics. The kinetic analysis of the Chou model revealed that the dehydrogenation process of the LMO-modified MgH_2 was transformed from penetration-controlled step to diffusion-controlled step. $\text{MgH}_2+9\text{wt}\%$ $\text{Ni}_3\text{Mn-LMO}$ started to release hydrogen at as low as $190\text{ }^\circ\text{C}$ and was able to release $6.59\text{wt}\%$ hydrogen in 5 min at a constant temperature of $295\text{ }^\circ\text{C}$. Even at as low as $250\text{ }^\circ\text{C}$ it was able to release $5.02\text{wt}\%$ hydrogen in 11 min, and the activation energy of dehydrogenation of $\text{MgH}_2+9\text{wt}\%$ $\text{Ni}_3\text{Mn-LMO}$ was reduced to $86.88\pm6.48\text{ kJ}\cdot\text{mol}^{-1}$. After 20 cycles, $\text{MgH}_2+9\text{wt}\%$ $\text{Ni}_3\text{Mn-LMO}$ still had a reversible capacity of $6.22\text{wt}\%$, exhibiting good cycling performance. Microstructural analysis illustrated that the high specific surface area of LMO, abundant active sites, reversible conversion of $\text{Mg}_2\text{Ni}/\text{Mg}_2\text{NiH}_4$, and multivalent chemical environment of Mn synergistically promoted the improvement of hydrogen storage performance of MgH_2 . And DFT calculations indicated that $\text{Mg}_2\text{Ni}/\text{Mg}_2\text{NiH}_4$ acted as a hydrogen pump to reduce the adsorption energy of hydrogen molecules on the MgH_2 surface and promote the dissociation of adsorbed hydrogen molecules into hydrogen atoms. In turn, the presence of manganese oxides can absorb electrons from $\text{Mg}_2\text{Ni}/\text{Mg}_2\text{NiH}_4$, producing a new DOS structure with lower d-bonding centers. This unique change further weakens the bond between hydrogen and $\text{Mg}_2\text{Ni}/\text{Mg}_2\text{NiH}_4$ leading to a further decrease in the energy barrier for hydrogen adsorption and dissociation. Our research provides a simple and efficient strategy to synthesize layered metal oxides with high specific surface area and high catalytic activity and demonstrates an effective method to improve the hydrogen storage properties of MgH_2 .

Declaration of competing interest

The authors declare no interest conflict. They have no known competing financial interests or personal relationships that could have appeared to influence the work reported in this paper.

CRediT authorship contribution statement

Tao Zhong: Writing – review & editing, Writing – original draft, Visualization, Methodology, Investigation, Data curation, Conceptualization. **Tian Xu:** Writing – original draft, Visualization, Data curation, Conceptualization. **Liuting Zhang:** Writing – review & editing, Resources, Funding acquisition. **Fuying Wu:** Writing – review & editing, Data curation. **Yiqun Jiang:** Writing – review & editing, Resources. **Xuebin Yu:** Writing – review & editing, Resources, Funding acquisition, Formal analysis.

Acknowledgments

The authors appreciatively acknowledge the financial supports from the National Key R&D Program of China (2020YFA0406204), the National Natural Science Foundation of China (Grant No 51801078).

Supplementary materials

Supplementary material associated with this article can be found, in the online version, at doi:[10.1016/j.jma.2024.04.027](https://doi.org/10.1016/j.jma.2024.04.027).

References

- [1] M. Song, L. Zhang, F. Wu, H. Zhang, H. Zhao, L. Chen, H. Li, J. Mater. Sci. Technol. 149 (2023) 99–111, doi:[10.1016/j.jmst.2022.11.032](https://doi.org/10.1016/j.jmst.2022.11.032).
- [2] L. Ren, Y. Li, N. Zhang, Z. Li, X. Lin, W. Zhu, C. Lu, W. Ding, J. Zou, Nano-Micro Lett. 15 (2023) 93, doi:[10.1007/s40820-023-01041-5](https://doi.org/10.1007/s40820-023-01041-5).
- [3] T. He, P. Pachfule, H. Wu, Q. Xu, P. Chen, Nat. Rev. Mater. 1 (2016) 16059, doi:[10.1038/natrevmats.2016.59](https://doi.org/10.1038/natrevmats.2016.59).
- [4] J. Yuan, H. Huang, Z. Jiang, Y. Lv, B. Liu, B. Zhang, Y. Yan, Y. Wu, ACS Appl. Nano Mater. 4 (2021) 1604–1612, doi:[10.1021/acsnano.0c02738](https://doi.org/10.1021/acsnano.0c02738).
- [5] T. Sadhasivam, H. Kim, S. Jung, S. Roh, J. Park, H. Jung, Renew. Sust. Energy Rev. 72 (2017) 523–534, doi:[10.1016/j.rser.2017.01.107](https://doi.org/10.1016/j.rser.2017.01.107).
- [6] N. Xu, K. Wang, Y. Zhu, Adv. Mater. 38 (2023) 2303173, doi:[10.1002/adma.202303173](https://doi.org/10.1002/adma.202303173).
- [7] X. Lu, L. Zhang, H. Yu, Z. Lu, J. He, J. Zheng, F. Wu, L. Chen, Chem. Eng. J. 422 (2021) 130101, doi:[10.1016/j.cej.2021.130101](https://doi.org/10.1016/j.cej.2021.130101).
- [8] L. Ren, Y. Li, Z. Li, X. Lin, C. Lu, W. Ding, J. Zou, Nano-Micro Lett. 16 (2024) 160, doi:[10.1007/s40820-024-01375-8](https://doi.org/10.1007/s40820-024-01375-8).
- [9] X.L. Zhang, Y.F. Liu, X. Zhang, J.J. Hu, M.X. Gao, H.G. Pan, Mater. Today Nano 9 (2020) 100064, doi:[10.1016/j.mtnano.2019.100064](https://doi.org/10.1016/j.mtnano.2019.100064).
- [10] Z. Ding, Y.T. Li, H. Yang, et al., J. Magnes. Alloy. 10 (2022) 2946, doi:[10.1016/j.jma.2022.09.028](https://doi.org/10.1016/j.jma.2022.09.028).
- [11] S. Li, Y. Zhu, Y. Liu, Y. Zhang, H. Lin, J. Zhang, W. Qiu, L. Li, J. Alloys Compd. 819 (2020) 153020, doi:[10.1016/j.jallcom.2019.153020](https://doi.org/10.1016/j.jallcom.2019.153020).
- [12] J. Cermak, L. Kral, P. Roupcova, Renew. Energy 188 (2022) 411, doi:[10.1016/j.renene.2022.02.021](https://doi.org/10.1016/j.renene.2022.02.021).
- [13] Y. Zhong, X.F. Wan, Z. Ding, L.L. Shaw, Int. J. Hydrog. Energy 41 (2016) 22104, doi:[10.1016/j.ijhydene.2016.09.195](https://doi.org/10.1016/j.ijhydene.2016.09.195).
- [14] G. Mulas, R. Campesi, S. Garroni, et al., J. Alloys Compd. 536 (2012) S236, doi:[10.1016/j.jallcom.2011.12.042](https://doi.org/10.1016/j.jallcom.2011.12.042).
- [15] Z. Lu, J. He, M. Song, Y. Zhang, F. Wu, J. Zheng, L. Zhang, L. Chen, Int. J. Min. Met. Mater. 30 (2023) 44–53, doi:[10.1007/s12613-021-2372-5](https://doi.org/10.1007/s12613-021-2372-5).
- [16] L. Wang, L. Zhang, X. Lu, F. Wu, X. Sun, H. Zhao, Q. Li, Chem. Eng. J. 465 (2023) 142766, doi:[10.1016/j.cej.2023.142766](https://doi.org/10.1016/j.cej.2023.142766).
- [17] J. Liu, Z. Ma, Z. Liu, Q. Tang, Y. Zhu, H. Lin, Y. Zhang, J. Zhang, Y. Liu, L. Li, Int. J. Hydrog. Energy 45 (2020) 16622–16633, doi:[10.1016/j.ijhydene.2020.04.104](https://doi.org/10.1016/j.ijhydene.2020.04.104).
- [18] H. Fu, J. Hu, Y. Lu, X. Li, Y. Chen, F. Pan, ACS Appl. Mater. Interfaces 14 (2022) 33161–33172, doi:[10.1021/acsmami.2c06642](https://doi.org/10.1021/acsmami.2c06642).
- [19] C. Duan, X. Wang, H. Wang, M. Wu, Y. Fan, J. Wu, T. Qu, B. Liu, L. Hu, P. Liang, F. Wang, Y. Wu, J. Mater. Sci. Technol. 189 (2024) 77–85, doi:[10.1016/j.jmst.2023.11.072](https://doi.org/10.1016/j.jmst.2023.11.072).
- [20] C. Duan, Y. Tian, X. Wang, J. Wu, B. Liu, D. Fu, Y. Zhang, W. Lv, L. Hu, F. Wang, X. Zhang, Y. Wu, Nano Energy 113 (2023) 108536, doi:[10.1016/j.nanoen.2023.108536](https://doi.org/10.1016/j.nanoen.2023.108536).
- [21] D. Gao, L. Zhang, M. Song, F. Wu, J. Wang, H. Zhao, H. Li, Int. J. Hydrog. Energy 25 (2023) 9390–9400, doi:[10.1016/j.ijhydene.2022.12.032](https://doi.org/10.1016/j.ijhydene.2022.12.032).
- [22] L. Zhang, F.M. Nyahuma, H. Zhang, C. Cheng, J. Zheng, F. Wu, L. Chen, Green Energy. Environ. 2 (2023) 589–600, doi:[10.1016/j.gee.2021.09.004](https://doi.org/10.1016/j.gee.2021.09.004).
- [23] S. Guemou, F. Wu, P. Chen, J. Zheng, T. Bian, D. Shang, A.P. Levtssev, L. Zhang, Int. J. Hydrog. Energy 62 (2023) 23943–23955, doi:[10.1016/j.ijhydene.2023.03.243](https://doi.org/10.1016/j.ijhydene.2023.03.243).
- [24] Y. Meng, S. Ju, W. Chen, X. Chen, G. Xia, D. Sun, X. Yu, Small Struct 10 (2022) 2200119, doi:[10.1002/sstr.202200119](https://doi.org/10.1002/sstr.202200119).
- [25] M. Chen, X. Xiao, M. Zhang, J. Mao, J. Zheng, M. Liu, X. Wang, L. Chen, Mater. Today Energy 16 (2020) 100411, doi:[10.1016/j.mtener.2020.100411](https://doi.org/10.1016/j.mtener.2020.100411).
- [26] K. Xian, M. Wu, M. Gao, S. Wang, Z. Li, P. Gao, Z. Yao, Y. Liu, W. Sun, H. Pan, Small 43 (2022) 2107013, doi:[10.1002/smll.202107013](https://doi.org/10.1002/smll.202107013).
- [27] C. Ning, S. Bai, J. Wang, Z. Li, Z. Han, Y. Zhao, D. O'Hare, Y. Song, Chem. Rev. 480 (2023) 215008, doi:[10.1016/j.ccr.2022.215008](https://doi.org/10.1016/j.ccr.2022.215008).
- [28] F. Wang, P. Zou, Y. Zhang, W. Pan, Y. Li, L. Liang, C. Chen, H. Liu, S. Zheng, Nat. Commun. 14 (2023) 6019, doi:[10.1038/s41467-023-41706-8](https://doi.org/10.1038/s41467-023-41706-8).
- [29] Y. Li, H. Guo, J. Zhao, Y. Zhang, L. Zhao, R. Song, Chem. Eng. J. 464 (2023) 142604, doi:[10.1016/j.cej.2023.142604](https://doi.org/10.1016/j.cej.2023.142604).
- [30] G. Huang, Y. Lu, X. Liu, W. Tang, X. Li, F. Wang, J. Shui, R. Yu, J. Magnes. Alloy (2023), doi:[10.1016/j.jma.2023.10.003](https://doi.org/10.1016/j.jma.2023.10.003).
- [31] Y. Wang, Q. Pan, Y. Qiao, X. Wang, D. Deng, F. Zheng, B. Chen, J. Qiu, Adv. Mater. 15 (2023) 2210871, doi:[10.1002/adma.202210871](https://doi.org/10.1002/adma.202210871).
- [32] D. Yang, J. Huang, Z. Hu, Y. Miao, F. Wang, Z. Zhang, Y. Xie, S. Liu, Q. Wang, C.U. Pittman, Fuel 357 (2024) 129982, doi:[10.1016/j.fuel.2023.129982](https://doi.org/10.1016/j.fuel.2023.129982).
- [33] X. Wang, J. Zhang, S. Yang, H. Yan, X. Hong, W. Dong, Y. Liu, B. Zhang, Z. Wen, Electrochim. Acta 295 (2019) 1–6, doi:[10.1016/j.electacta.2018.10.021](https://doi.org/10.1016/j.electacta.2018.10.021).
- [34] L. Qiao, C. Xi, C. Li, K. Zhang, Q. Li, J. Han, Y. Ding, Adv. Funct. Mater. (2024) 2402286, doi:[10.1002/adfm.202402286](https://doi.org/10.1002/adfm.202402286).
- [35] C. Yuan, J. Li, L. Hou, X. Zhang, L. Shen, X. (David) Lou, Adv. Funct. Mater. 21 (2012) 4592–4597, doi:[10.1002/adfm.201200994](https://doi.org/10.1002/adfm.201200994).
- [36] K. Kalantar-zadeh, J. Ou, T. Daeneke, A. Mitchell, T. Sasaki, M.S. Fuhrer, Appl. Mater. Today 5 (2016) 73–89, doi:[10.1016/j.apmt.2016.09.012](https://doi.org/10.1016/j.apmt.2016.09.012).
- [37] K. Chou, Q. Li, Q. Lin, L. Jiang, K. Xu, Int. J. Hydrog. Energy 3 (2005) 301–309, doi:[10.1016/j.ijhydene.2004.04.006](https://doi.org/10.1016/j.ijhydene.2004.04.006).
- [38] E. Xu, H. Li, X. You, C. Bu, L. Zhang, Q. Wang, Z. Zhao, Int. J. Hydrog. Energy 12 (2017) 8057–8062, doi:[10.1016/j.ijhydene.2016.12.102](https://doi.org/10.1016/j.ijhydene.2016.12.102).
- [39] B. Zhang, X. Xie, Y. Wang, C. Hou, X. Sun, Y. Zhang, X. Yang, R. Yu, W. Du, J. Magnes. Alloy (2022), doi:[10.1016/j.jma.2022.07.004](https://doi.org/10.1016/j.jma.2022.07.004).
- [40] C. Mochizuki, Y. Inomata, S. Yasumura, M. Lin, A. Taketoshi, T. Honma, N. Sakaguchi, M. Haruta, K. Shimizu, T. Ishida, T. Murayama, ACS Catal. 12 (2022) 6149–6158, doi:[10.1021/acscatal.2c00108](https://doi.org/10.1021/acscatal.2c00108).
- [41] L. Dong, G. Chang, Y. Feng, X. Yao, X. Yu, Rare Metals 41 (2022) 1583–1594, doi:[10.1007/s12598-021-01881-3](https://doi.org/10.1007/s12598-021-01881-3).
- [42] M. Sun, J. Wang, J. Mater. Chem. A 11 (2023) 21420–21428, doi:[10.1039/D3TA03473A](https://doi.org/10.1039/D3TA03473A).
- [43] S. Shen, L. Ouyang, J. Liu, H. Wang, X. Yang, M. Zhu, J. Magnes. Alloy 9 (2023) 3174–3185, doi:[10.1016/j.jma.2021.12.003](https://doi.org/10.1016/j.jma.2021.12.003).
- [44] H. Jia, Y. Li, L. Fu, U. Ali, B. Liu, L. Zhang, H. Wang, L. Li, H. Wang, C. Wang, Small 46 (2023) 2303593, doi:[10.1002/smll.202303593](https://doi.org/10.1002/smll.202303593).

- [45] X. Li, Q. Zhou, Z. Yang, X. Zhou, D. Qiu, H. Qiu, X. Huang, Y. Yu, Energy. Environ. Mater. 3 (2023) e12378, doi:[10.1002/eem2.12378](https://doi.org/10.1002/eem2.12378).
- [46] J..K. Nørskov, F. Studt, F. Abild-Pedersen, T. Bligaard, Angew. Chem. Int. Edit. 54 (2015) 10404–10405, doi:[10.1002/anie.201506018](https://doi.org/10.1002/anie.201506018).
- [47] L. Ren, W. Zhu, Q. Zhang, C. Lu, F. Sun, X. Lin, J. Zou, Chem. Eng. J. 434 (2022) 134701, doi:[10.1016/j.cej.2022.134701](https://doi.org/10.1016/j.cej.2022.134701).
- [48] X. Zhang, Y. Sun, S. Ju, J. Ye, X. Hu, W. Chen, L. Yao, G. Xia, F. Fang, D. Sun, X. Yu, Adv. Mater. 2 (2023) 2206946, doi:[10.1002/adma.202206946](https://doi.org/10.1002/adma.202206946).